PAPER

Check for updates

Direct oxidation of methane to methanol using CuMoO₄†

Wenjian Wu,[a] Wenzhi Li, ⓘ *[ab] Mingwei Wu,[a] Hao Zhang,[a] Chen Zhu[a] and Yihang Jiang[a]

Upgrading methane into methanol or other high value-added chemicals is not only beneficial to mitigate the greenhouse effect, but also provides basic raw materials for industrial production. Nowadays, most research is limited to zeolite systems, and it is a considerable challenge to extend the support to metal oxides while achieving a high yield of methanol. In this paper, we take advantage of impregnation methods to synthesise a novel Cu/MoO₃ catalyst, which can convert methane to methanol in the gaseous phase. At 600 °C, the Cu(2)/MoO₃ catalyst can achieve a maximum STY$_{CH_3OH}$ of 47.2 μmol (g^{-1} h^{-1}) with a molar ratio $CH_4 : O_2 : H_2O = 5 : 1.4 : 10$. Consequences of SEM, TEM, HRTEM and XRD substantiate that Cu is incorporated into the lattice of MoO₃ to form CuMoO₄. And transmission infrared spectroscopy, Raman spectroscopy together with XPS characterization techniques confirm the generation of CuMoO₄, which is the main active site provider. This work provides a new support platform for Cu-based catalyst research in the methane-to-methanol system.

1. Introduction

Today, achieving carbon neutrality is both the ambitious vision of people worldwide and an important goal for individual countries.[1,2] In this process, a series of energy sources with the main component of methane, such as natural gas, combustible ice, coal-bed methane, biogas, *etc.*, play an indispensable role. Compared with traditional fossil energy, these energy reserves are larger, more widely distributed and more environmentally friendly when used.[3,4] However, in the process of resource extraction, a large amount of methane is inevitably produced. Simultaneously, since the global warming capacity of methane is more than 20 times that of carbon dioxide, direct emissions or inefficient utilization will cause serious greenhouse effects.[5,6] At present, the most ideal treatment is to convert methane into methanol and other high value-added chemicals, which has the superiority of increasing energy density, facilitating storage and transportation, while also providing raw materials for modern industry.[7,8] But due to its symmetrical regular tetrahedral structure, the energy of breaking C–H chemical bond is higher than that in methanol,[9,10] which makes the direct conversion of methane to methanol difficult to achieve. Therefore, in industrial production, steam reforming is the dominating method in methane transformation.[11,12] At 1123–

1173 K and 30 bar, methane is first converted to CO and H₂, then the syngas is converted to methanol. For this process, firstly, it is energy-intensive and requires a lot of large-scale facilities, which is not environmental-friendly. Second, it is a multi-step process and there is an upper limit to the conversion efficiency.[13,14] Considering these drawbacks, we urgently need a catalyst to realize the single-step conversion of methane to methanol with low energy consumption.

In recent years, precious metal catalysts and zeolite catalysts are the two main research directions.[15,16] A series of noble metal catalysts including Au,[17,18] Pd,[19,20] Rh (ref. 21 and 22) and Ir (ref. 23) usually have a good promotion effect on the adsorption of methane and the cleavage of the C–H bond. However, their scarcity and expensive price attribute limit their large-scale application. Zeolite catalysts originated from mimicking methane monooxygenase (MMO) in nature, which can use methane, oxygen and water to produce methanol in a moderate temperature and normal pressure.[24,25] Through simulating the structure of MMO, many scientists have loaded Cu or Fe onto zeolite including mordenite (MOR),[26–29] chabazite (CHA)[30–32] and ZSM-5 (ref. 33–35) by impregnation or ion exchange methods. For Fe-zeolite catalysts, its biggest limitation is that its oxidant is mainly N₂O[36,37] or H₂O₂.[38,39] Neither N₂O nor H₂O₂ are available directly from nature, and they are also much more expensive than the product methanol. And Cu-zeolite catalysts have the most industrial research value due to its large reserves, low price, and the ability to use oxygen as an oxidant. But due to the poor hydrothermal stability of ordinary silica–alumina zeolites, and its many Brønsted acid and Lewis acid sites, which are not conducive to the desorption of methanol.[40,41] Many scientists

[a]*Laboratory of Clean Low-Carbon Energy, University of Science and Technology of China, Hefei 230023, PR China. E-mail: liwenzhi@ustc.edu.cn; Fax: +86 0551 63600786; Tel: +86 0551 63600786*

[b]*Institute of Energy, Hefei Comprehensive National Science Center, Hefei 230031, PR China*

hope to expand the application of the carrier. Ha V. Le *et al.* used the impregnation method to support Cu on SBA-15 and found that the highly dispersed CuO particles have the ability to catalyze methane to methanol.[42] S. E. Bozbag *et al.* prepared Cu–SiO$_2$ catalyst, and the active Cu-oxo sites were formed on its surface that can help with methane activation.[43] Liu, Z. *et al.* synthesized CeO$_2$–Cu$_2$O catalyst and they also emphasized that water plays a key role in promoting methanol production.[44] Other materials also have potential as Cu catalyst supports.

Some studies have shown that MoO$_3$ is a promising and valuable catalyst carrier.[45,46] MoO$_3$ has multiple valence states (+6, +5 and +4) and abundant oxygen vacancies, which enable it to possess favorable dehydrogenation and oxygenation capacity. For example, H.-F. Liu *et al.* synthesized Mo/SiO$_2$ catalyst, which used N$_2$O to form Mo^{6+}O^{2-} that could convert CH$_4$ to HCHO.[47] K. Aoki *et al.* prepared MoO$_3$/SiO$_2$ catalyst using sol–gel method. With excess water vapor, methane was partially oxidized to methanol and formaldehyde.[48] Through the metal–support interaction, the MoO$_3$ support can easily interact with other metals to produce specific reactive species, thereby improving the activity. For example, C. Brookes *et al.* prepared a core–shell Fe$_2$O$_3$–MoO$_3$ catalyst to selectively convert methanol to formaldehyde.[49] They confirmed that ferric molybdate is the active component for formaldehyde synthesis. J. Zhu *et al.* synthesized a series of M$_x$O$_y$/MoO$_3$/CeO$_2$ (M = Ni, Cu, Fe) catalyst for selective reduction of NH$_3$ and NO.[50] In addition, MoO$_3$ also has the advantages of low cost and good chemical stability, which help it widely used in catalytic conversion. These advantages demonstrate the potential of MoO$_3$ as a carrier to help convert methane into methanol.

Taking the above factors into consideration, we prepared a novel Cu/MoO$_3$ catalyst by impregnation method. And Cu was uniformly dispersed on the carrier and formed active species of CuMoO$_4$, which can catalyze the synthesis of methanol from methane, oxygen and water. The influences of various reaction parameters such as Cu wt%, reaction temperature, molar ratio of CH$_4$–O$_2$–H$_2$O on methanol yield were discussed. Different characterization methods such as BET, ICP-AES, TEM, SEM, XRD, XPS are adopted to research the structure and properties of Cu/MoO$_3$ catalyst. Simultaneously, transmission infrared spectroscopy (TS) and Raman spectroscopy are exploited to study the active component of Cu/MoO$_3$ catalyst and CuMoO$_4$ is convinced to be the main active site supplier.

2. Experimental

2.1. Materials

Molybdenum trioxide (MoO$_3$, 99.95%) and cupric carbonate basic were purchased from Shanghai Aladdin Biochemical Technology Co., Ltd. Ammonium carbonate and ammonia solution (25–28%) were purchased from Sinopharm Chemical Reagent Co., Ltd. All of materials were applied without further purification.

2.2. Catalysts preparation

The Cu/MoO$_3$ catalysts were compounded by impregnation method. First, 2.5 g of ammonium carbonate was added into

10 mL of ammonia water with stirring to make a pellucid solution. Then, putting 3 g of cupric carbonate basic into the previous solution. After stirring at 800 rpm for 30 min, the precursor solution was prepared. Cu/MoO$_3$ catalysts with different mass fractions were synthesized by mixing the MoO$_3$ carrier with an appropriate amount of the precursor solution. Afterwards, the catalysts were placed in an oven to dry overnight at 150 °C following by calcining at 400 °C in the muffle furnace. Therefore, the Cu(x)/MoO$_3$ catalysts were prepared successfully, where the x represented the mass fraction of Cu.

2.3. Characterization

The structure and physicochemical properties were investigated by inductively coupled plasma atomic emission spectrometer (ICP-AES), Brunauer–Emmett–Teller method (BET), transmission electron microscope (TEM), high-resolution transmission electron microscope (HRTEM), scanning electron microscope (SEM), X-ray diffraction (XRD), X-ray photoelectron spectroscopy (XPS), transmission infrared spectroscopy (TS), hydrogen-temperature programmed reduction (H$_2$-TPR), UV-vis spectroscopy and Raman spectroscopy (Raman). A detailed description of the characterization techniques was given in the ESI.†

2.4. Catalyst activity test

The reactive gas included 15% CH$_4$ (residual gas is N$_2$) and synthetic air (abbreviated as air, 21% O$_2$ + 79% N$_2$). Activity tests of Cu/MoO$_3$ catalysts were carried out in fixed bed reactors at atmospheric pressure. The schematic diagram of the reaction device is shown in Fig. S1.† At first, 50 mg of the testing sample was placed in the middle of the quartz tube (i.d. 6 mm). And quartz wool was used as a fixture to prevent it from being blown away by the reaction gas. Secondly, heated the furnace to the corresponding temperature (400 °C, 450 °C, 500 °C, 550 °C, 600 °C) at a heating rate of 10 °C min^{-1} and catalyst was activated for one hour at this temperature. After that, CH$_4$ and air were introduced into the quartz tube, and their flow rates were controlled by flowmeters respectively. Then, controlled the precise amount of water entering the reaction chamber with a water vapor generator. Unless specifically mentioned, all the response time had been set to two hours and the water inlet speed were set to 3 μL min^{-1}. Finally, the outlet gas first passed through the cold trap (set at −3 °C) following by entering the gas chromatograph (GC) for online analysis. The gas chromatography utilized an HP-PLOT/Q column to separate the products and a flame ionization detector (FID) to detect the signal of the products. Selectivity of liquid products as well as yield were analyzed by calibrated GC and nuclear magnetic resonance hydrogen spectroscopy (^{1}H-NMR). The methanol space-time yield (STY) was computed as $N_{\text{CH}_3\text{OH}}/(M_{\text{cat}} \times T)$, where $N_{\text{CH}_3\text{OH}}$ represented the molar amount of methanol collected in the cold trap, M_{cat} represented the mass of the catalyst and T represented the reaction time. The selectivity of each liquid product was calculated as $S_{\text{CH}_3\text{OH}} = N_{\text{CH}_3\text{OH}}/(N_{\text{CH}_3\text{OH}} + N_{\text{CH}_3\text{OOH}} + N_{\text{OHCH}_2\text{OOH}})$, $S_{\text{CH}_3\text{OOH}} = N_{\text{CH}_3\text{OOH}}/(N_{\text{CH}_3\text{OH}} + N_{\text{CH}_3\text{OOH}} + N_{\text{OHCH}_2\text{OOH}})$ and $S_{\text{OHCH}_2\text{OOH}} = N_{\text{OHCH}_2\text{OOH}}/(N_{\text{CH}_3\text{OH}} + N_{\text{CH}_3\text{OOH}} +$

N_{OHCH_2OOH}), where N_{CH_3OOH} represented the molar amount of CH_3OOH and N_{OHCH_2OOH} represented the molar amount of $OHCH_2OOH$.

3. Results and discussion

3.1. Crystal structure and morphology

Table S1† lists the results of ICP-AES and BET characterization techniques. From the ICP-AES data, there is no difference between the theoretical value and the actual value of Cu loading, which proves the accuracy of the previous preparation process. Analysis of the BET data shows that with the increase of Cu loading, the specific surface area and pore volume of the catalyst also increase gradually. This result confirms that Cu is supported on MoO₃ and has an effect on the surface properties of MoO₃. There are two possibilities. One is that the agglomeration of Cu on the surface of MoO₃ increases the specific surface area and pore size, and the other is that the incorporation of Cu destroys the initial morphology of MoO₃ and reacts with it to form a new species, which is confirmed by the results of XRD and SEM.

Fig. 1 exhibits the XRD patterns of different Cu/MoO₃ catalysts. In Fig. 1A, the main peaks of catalysts loaded with different Cu mass fractions are analogous, which correspond to α-MoO₃ (orthorhombic MoO₃, JCPDS PDF #35-0609). α-MoO₃ is a thermodynamically stable phase structure that can interact with other metal ions and maintain its own structure without drastic changes. Therefore, when the Cu loading increased from 0% to 11%, the XRD signal of samples do not change much. And the diffraction peaks of CuO has not appeared, which means that Cu is very uniformly distributed on the MoO₃ carrier or Cu enters the lattice of MoO₃ to form new species. Fig. 1B exhibits the XRD pattern features between 20–30°. As can be seen from the Fig. 1B, when Cu is impregnated on the support, the sharpness of these peaks decreased to a certain extent. This

phenomenon indicates that Cu has interacted with MoO₃ carrier and influences its crystallinity. New peaks appear in the XRD patterns of Cu(3)/MoO₃, Cu(5)/MoO₃, Cu(11)/MoO₃, which correspond to CuMoO₄ (JCPDS PDF #22-0242). This metal compound has been verified to provide multiple active sites to catalyze the oxidation of methane, formaldehyde and other species.[50–52]

Fig. 2 displays the SEM images of the Cu/MoO₃ catalysts. Typical morphology of commercial MoO₃ without Cu loading is in the form of irregular polygons, which is presented in Fig. 2a. With the addition of Cu, this morphology is destroyed gradually. And when the Cu loading reaches 11%, the morphology is basically completely destroyed and transformed into smaller irregular polygons (Fig. 2f). According to the above phenomenon, we can infer that Cu is not simply loaded on MoO₃, but is likely to interact with the support to form new species and produce dissimilar appearances.

The TEM results of different Cu/MoO₃ catalysts are shown in Fig. S2.† Analysis of the TEM images show that although Cu is impregnated on the MoO₃ support, even if the catalyst is Cu(11)/MoO₃, there are still no obvious particles on the surface of the sample. This indicates that Cu is very likely to enter the lattice of MoO₃ and form new species. Fig. 3 exhibits the HRTEM image and element mapping of Cu(2)/MoO₃. Fig. 3a shows two typical crystal planes ((1 1 0), (0 4 1)) of α-MoO₃, which are consistent with the XRD results. And Fig. 3b reveals the distribution of Mo, O, Cu elements on the catalyst surface. As shown in the picture, the Cu element is dispersed uniformly and no apparent aggregation can be noticed. Combined with the results of XRD, SEM, TEM, etc., after Cu is supported on the MoO₃ carrier, Cu is capable of interacting with the carrier and entering the lattice of MoO₃, thereby forming new species of CuMoO₄, which possesses the active sites of methane oxidation probably.

H₂-TPR experiments are performed to probe the redox capacity of the dissimilar catalysts. The specific data is shown in
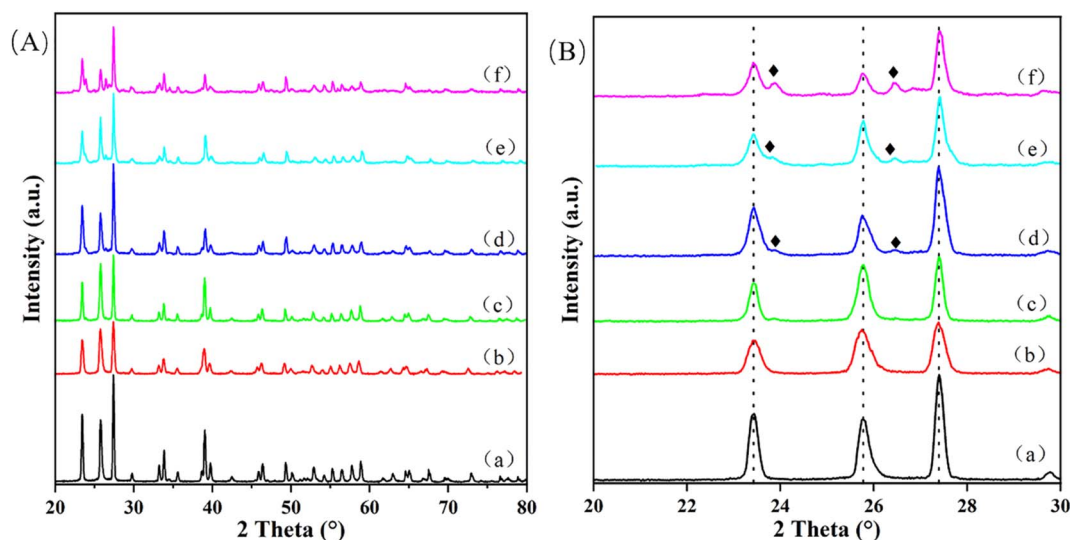

Fig. 1 (A) 20–80° XRD patterns of (a) Cu(0)/MoO₃, (b) Cu(1)/MoO₃, (c) Cu(2)/MoO₃, (d) Cu(3)/MoO₃, (e) Cu(5)/MoO₃, (f) Cu(11)/MoO₃; (B) 20–30° XRD patterns in (A). (◆) represents CuMoO₄.

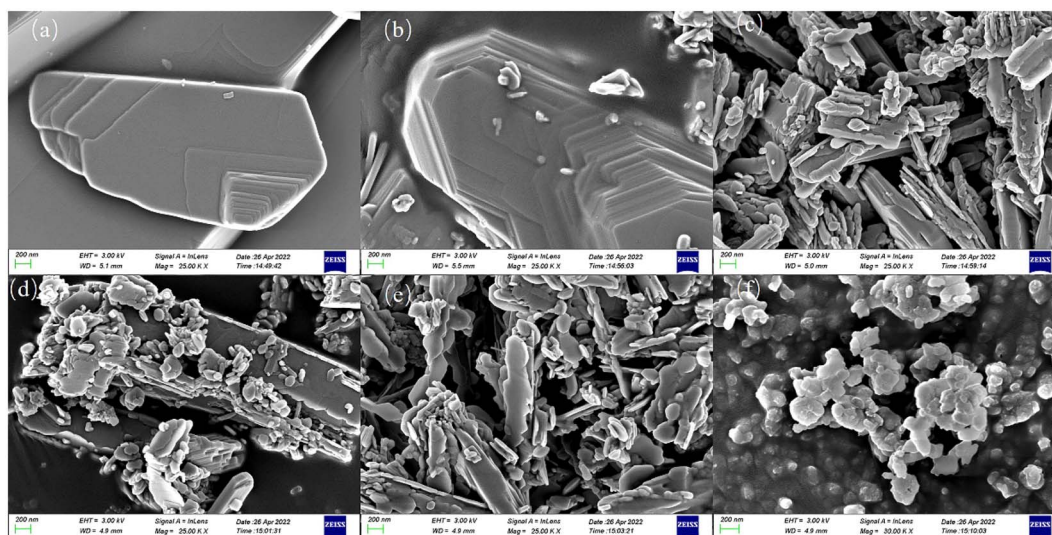**Fig. 2** SEM images of (a) Cu(0)/MoO$_3$, (b) Cu(1)/MoO$_3$, (c) Cu(2)/MoO$_3$, (d) Cu(3)/MoO$_3$, (e) Cu(5)/MoO$_3$, (f) Cu(11)/MoO$_3$.

Fig. 4. For purified MoO$_3$ catalyst, the reduction peak appears only at 657 °C, which correspond to the reduction of Mo^{6+} to Mo^{5+} and Mo^{4+}.[51,53,54] After Cu had supported on the carrier, the reduction temperature drops sharply. Simultaneously, a distinct shoulder peak at 492 °C also appears, which can be viewed as the reduction of Mo^{6+} in CuMoO$_4$. So it is obvious that the incorporation of Cu helps the formation of new active species on the catalyst surface, which is consistent with the results of XRD, SEM and TEM. With the increasing mass fraction of Cu, the reduction temperature shows a downward trend. And new reduction peak is shown at near 370 °C, which can be assigned to the reduction of tiny copper oxide.[55,56] When Cu
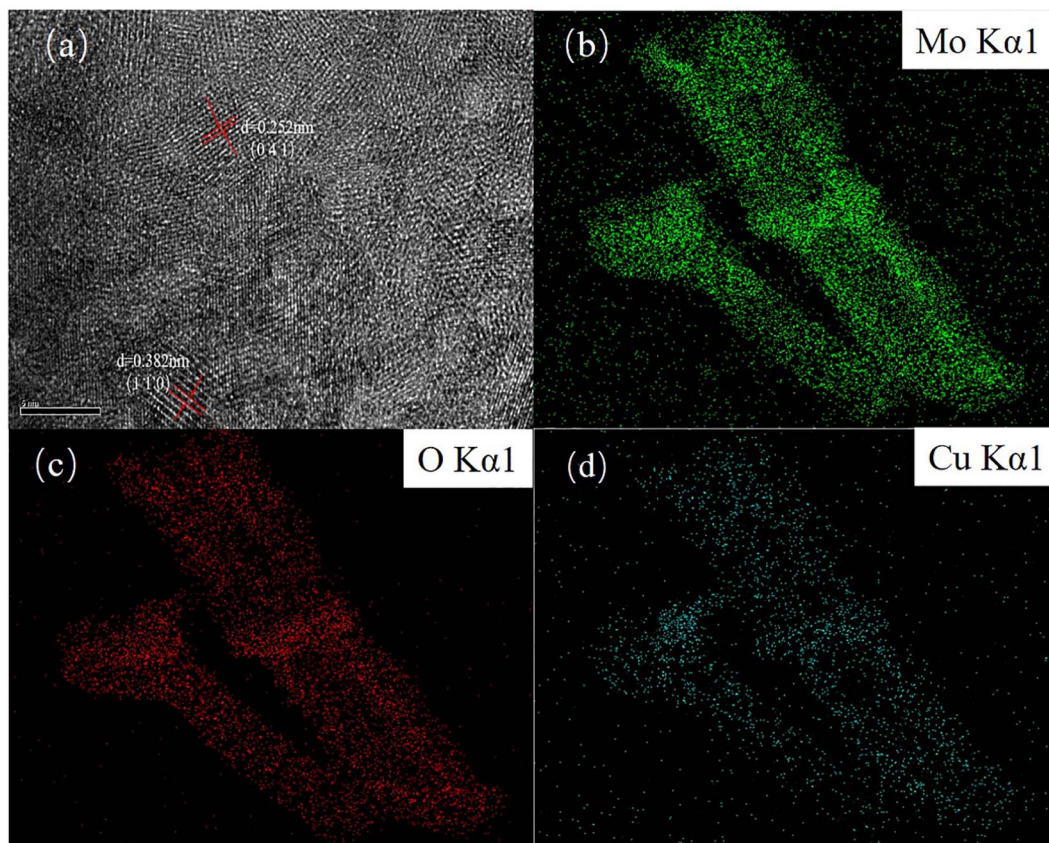

Fig. 3 (a) HRTEM image and (b–d) EDX element mapping of the Cu(2)/MoO$_3$ catalyst.
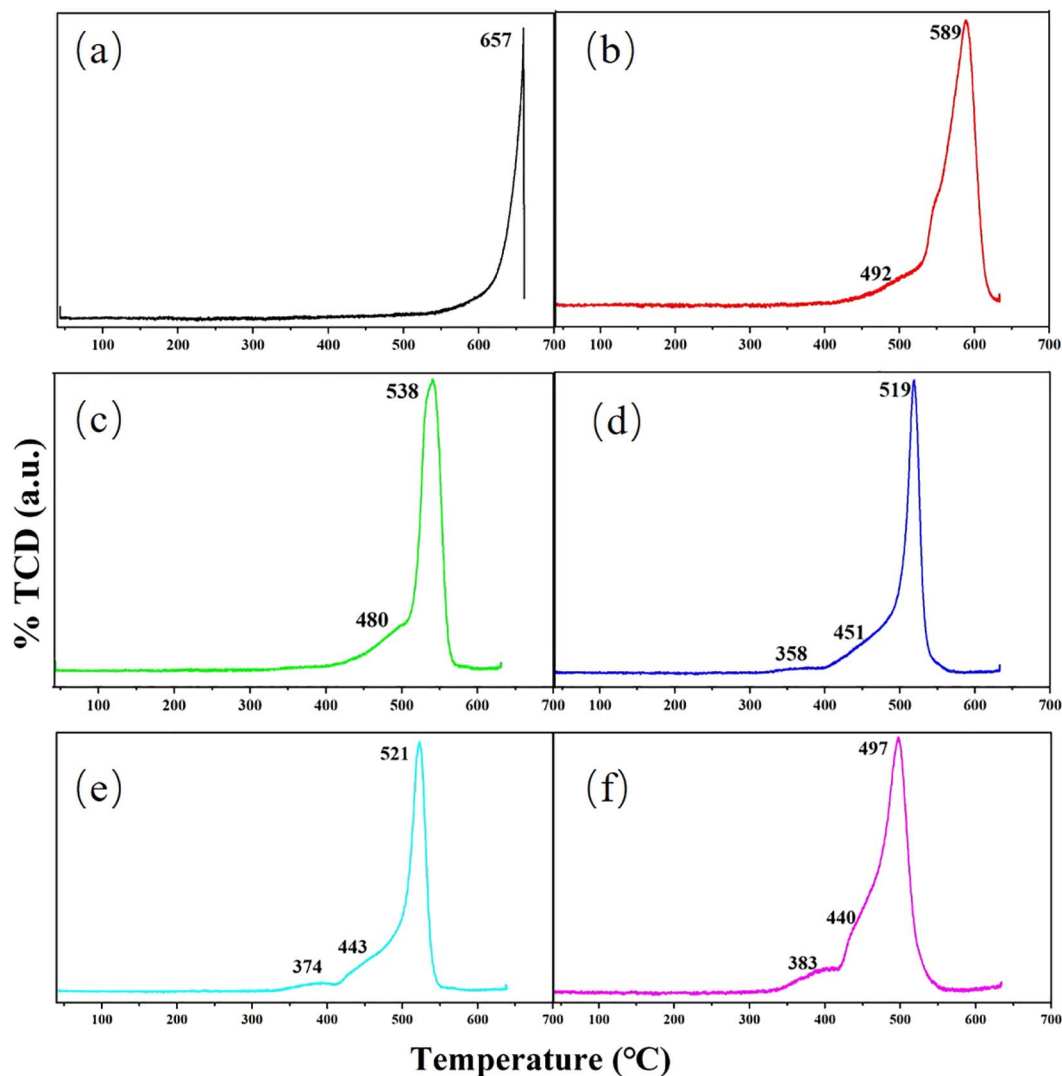
Fig. 4 TPR profiles of H_2 for (a) Cu(0)/MoO$_3$, (b) Cu(1)/MoO$_3$, (c) Cu(2)/MoO$_3$, (d) Cu(3)/MoO$_3$, (e) Cu(5)/MoO$_3$, (f) Cu(11)/MoO$_3$.

loading increases from 0 wt% to 1 wt% and 1 wt% to 2 wt%, the drop in temperature is very large, close to 60 °C. After that, the temperature drop becomes smaller, which means that there is an upper limit for the influence of Cu on the redox properties of the carrier itself. J. L. Brito *et al.* prepared Ni–Mo oxides and found that Ni and Mo had an optimal ratio, excess Ni would produce tiny NiO.[57] W. Yu *et al.* investigated the surface structure of CuO/MoO$_3$/CeO$_2$ and demonstrated that the amount of Cu should be regulated, excess Cu would produce tiny copper oxides.[58] Combining with the phenomenon that new reduction peak appears at near 370 °C in Fig. 4d–f, the optimal loading of Cu may be 2 wt%. This finding has great guiding significance for the influence of Cu mass fraction on methanol yield.

3.2. Catalyst activity

The effects of Cu loading together with reaction temperature on the STY$_{CH_3OH}$ and liquid product selectivity are studied preliminary and the consequences are shown in Fig. 5 and Table S2.† And the ^{1}H-NMR result of liquid products is shown in

Fig. S3,† from which we can find that CH$_3$OH, CH$_3$OOH and OHCH$_2$OOH are the main component. From Fig. 5a and Table S2,† we can find that in the absence of Cu incorporation, the reactivity of the Cu(0)/MoO$_3$ is very deficient. After Cu is impregnated on the support, the methanol yield is improved significantly. With the increase of Cu mass fraction, the methanol yield reached the optimum value at Cu(2)/MoO$_3$, and then the number began to decrease. As to the selectivity, when the mass fraction of Cu was less than 2 wt%, the selectivity of the three products was basically the same. But when the mass fraction of Cu increased to 3 wt%, the S_{OHCH_2OOH} became higher, while the S_{CH_3OH} and S_{CH_3OOH} decreased. Even after the copper loading exceeded 5 wt%, OHCH$_2$OOH was basically undetectable, indicating that excessive oxidation had occurred in the reaction. From the results of H_2-TPR, we can know that when the loading of Cu exceeds 2 wt%, there will be tiny copper oxides produced. And since methane has a symmetrical regular tetrahedral configuration, the energy required to break its C–H bond is much higher than the energy required to break the C–H
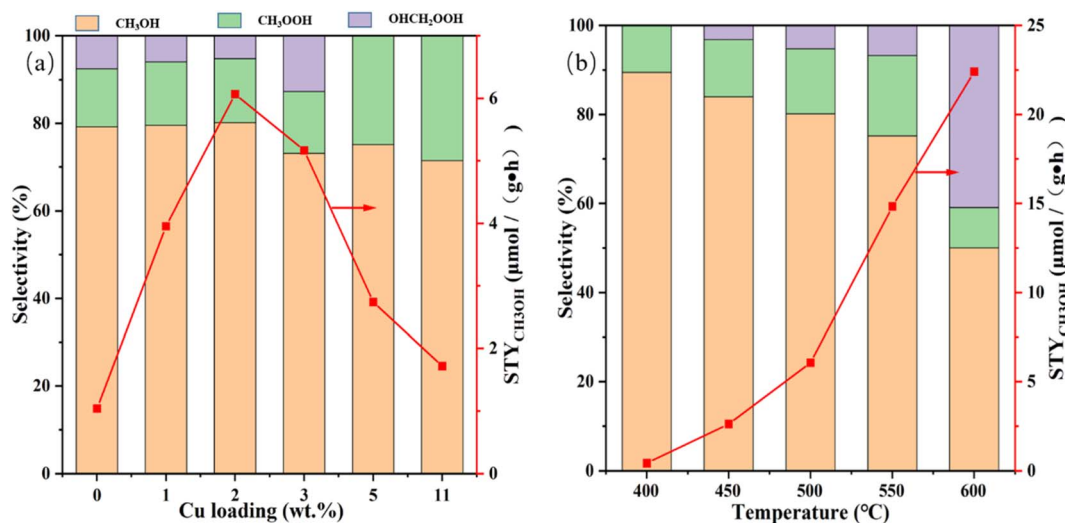
Fig. 5 (a) Effect of Cu loading on STY_{CH_3OH} and methanol selectivity. Reaction conditions: T = 500 °C, $CH_4 : O_2 : H_2O$ = 4 : 2.8 : 10. (b) Effect of reaction temperature on STY_{CH_3OH} and methanol selectivity of Cu(2)/MoO$_3$. Reaction conditions: $CH_4 : O_2 : H_2O$ = 4 : 2.8 : 10.

bond in methanol, which leads to the liable over-oxidation of intermediate product and methanol.[59,60] Therefore, for Cu(3)/MoO$_3$, Cu(5)/MoO$_3$ and Cu(11)/MoO$_3$ catalysts, the intermediate products of the reaction and methanol are highly likely to have more severe over-oxidation, which leads the decrease of methanol yield. Because the Cu(2)/MoO$_3$ catalyst maintains the best activity, we mainly study this sample next. The influence of reaction temperature on the Cu(2)/MoO$_3$ catalyst is shown in Fig. 5b and Table S2.† Elevating temperature has a positive effect on methanol yield. When the temperature reaches 600 °C, the methanol yield reaches 22.4 μmol (g^{-1} h^{-1}). However, the selectivity of methanol and CH$_3$OOH gradually decreases, while the proportion of OHCH$_2$OOH gradually increase, indicating that with the increase of temperature, the reaction product will undergo a certain excessive oxidation phenomenon. Because our target is to achieve higher methanol space-time yield, the positive effect of increasing temperature on methanol yield outweighs the negative impact of excessive methanol oxidation, we choose 600 °C as the optimal temperature for the reaction. And Fig. S4† displays the thermogravimetric analysis (TGA) result of Cu(2)/MoO$_3$. According to this picture, when temperature arrives at 658 °C, the sample will become unstable and begin to evaporate and decompose gradually. That's why we set the maximum reaction temperature to 600 °C. Within 400–600 °C, the higher the reaction temperature, the better the activity. It is well-known that the high temperature provides more energy to activate methane molecules while speeding up the reaction rate. And it may also help to increase the catalytic active sites. More characterization methods will be adopted to investigate this intrinsic reason.

3.3. Surface chemical groups

The UV-vis spectra of Cu(2)/MoO$_3$ catalyst at different temperature are shown in Fig. S5.† In Cu-zeolite catalysts, the peak at 22 700 cm^{-1} is often considered the active site in the methane-

to-methanol reaction, but this is not shown in Fig. S5.†[61,62] And there are no other signature peak signals for active copper species. Therefore, the active species in Cu/MoO$_3$ catalyst are not the same as the active species in zeolite.

Transmission infrared spectroscopy (TS) is applied to further study the specific structure of the Cu/MoO$_3$ catalyst. And the spectrum is performed in Fig. 6. The peak at 522 cm^{-1} and the peak in the range 739–829 cm^{-1} can be considered to be aroused by the vibration of the Mo–O–Mo bond. At the same
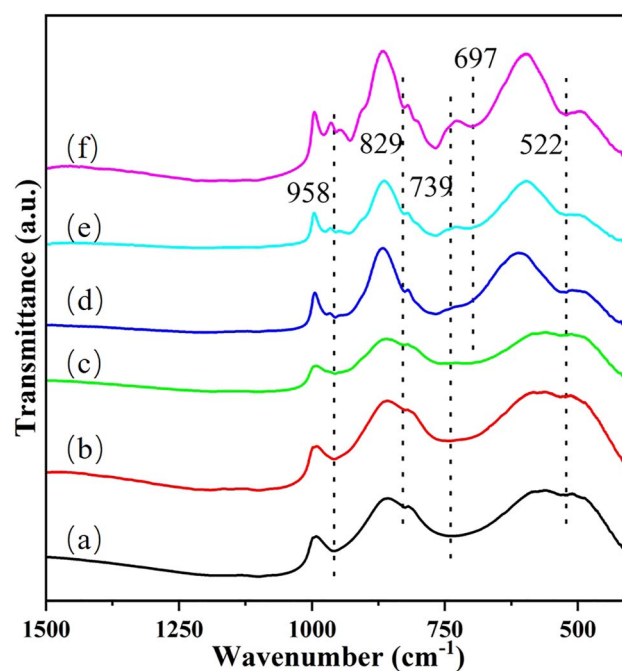

Fig. 6 Transmitted infrared spectroscopy (TS) images of (a) Cu(0)/MoO$_3$, (b) Cu(1)/MoO$_3$, (c) Cu(2)/MoO$_3$, (d) Cu(3)/MoO$_3$, (e) Cu(5)/MoO$_3$, (f) Cu(11)/MoO$_3$.

time, the peak at 958 cm^{-1} represents the vibration of terminal Mo=O bond in bulk MoO$_3$.[49,63,64] With the doping of Cu, the peak near 739 cm^{-1} is slightly shifted firstly, which means that Cu atoms may have contact with Mo atoms and then affect the Mo–O–Mo bond. Secondly, a new vibrational peak appears at 697 cm^{-1} which represents the formation of Cu–O–Mo bond. Thirdly, two shoulder peaks generate around the peak of 958 cm^{-1}, which are correspond to the vibration of Mo=O bond in the molybdate ion.[52,65] Combined with the above results, it is obvious that Cu interacts with the MoO$_3$ after being dispersed on its surface and forms new species. Basing on the previous analysis, the new species is CuMoO$_4$. Although the change of each vibration peak is not very distinct in Cu(1)/MoO$_3$ and Cu(2)/MoO$_3$, the following Raman spectroscopy will prove that the two also produced new species.

Fig. S6 and S7† illustrate the Raman spectra of Cu/MoO$_3$ catalysts under different conditions. The spectral range of Fig. S6† is 500–1100 cm^{-1}. As we can discovery in the spectra, there are three foremost peaks presented at 667 cm^{-1}, 819 cm^{-1} and 997 cm^{-1}. The peak at 667 cm^{-1} is assigned to the symmetric stretching vibrations of Mo–O–Mo in bulk MoO$_3$, the peak at 819 cm^{-1} is a typical Mo–O–Mo asymmetric stretch and the band at 997 cm^{-1} is originally from terminal vibration of Mo=O in bulk MoO$_3$.[50,66,67] But due to the support of the catalyst is commercial MoO$_3$, its own signal is too strong and do not transform severely, resulting in less obvious peaks of other species. Simultaneously, indistinct peak signal appeared between 860–980 cm^{-1}, so we analyze this part of the Raman spectra. The detailed spectra are shown in Fig. 7. In Fig. 7A, three major peaks are appeared at 888 cm^{-1}, 937 cm^{-1}, 968 cm^{-1}, which are characteristic peaks of CuMoO$_4$.[51,52,68] The band at 968 cm^{-1} can be recognized as the stretching mode of terminal Mo=O bond in the molybdate ion, the band at 937 cm^{-1} is aroused from the asymmetric vibration of Mo=O in the distorted tetrahedral structure and the peak at 888 cm^{-1} is correspond to the stretching vibration of Mo–O bond. With the impregnation of Cu on the carrier, these peaks become more intense gradually. And in the Cu(2)/MoO$_3$ catalyst, the signals are exhibited clearly. This phenomenon has convinced that Cu/MoO$_3$ catalyst with different Cu loading all possess this new species. The conclusion obtained from the Raman spectrum in

Fig. 7A is mutually confirmed with the completion acquired from the Fig. 6.

Effect of reaction temperature is shown in Fig. 7B. As we can see from this picture, the characteristic peaks about CuMoO$_4$ put in an appearance again. The intensity of these governing signals gradually strengthens with the increase of reaction temperature. According to Fig. 5b, the methanol yield is also enhanced with temperature getting higher. Thence, we can conjecture that CuMoO$_4$ has a significant impact on the catalyst activity. Higher temperature makes more Cu interact with MoO$_3$ support to form more CuMoO$_4$, which helps the manufacture of methanol. Comparing with Fig. 7A, although more CuMoO$_4$ are produced with more Cu loading. But according to the results of H$_2$-TPR, we can also know that tiny copper oxides also appeared. This may cause more severe over-oxidation and reduce methanol yield.

Fig. 7C reveals the evolution of surface active species on Cu(2)/MoO$_3$ catalysts under different reaction atmosphere. The intensity of the three peaks gradually decreases from top to bottom, as the reactant gas changes from air to 15% CH$_4$ + air following by only 15% CH$_4$. At the beginning, only sending air into the reaction line helps the fabrication of CuMoO$_4$. Then when the 15% CH$_4$ is pouring into the tube simultaneously, the peak intensity decreases obviously, which means the consumption of CuMoO$_4$. Finally, only 15% CH$_4$ is blowing into the quartz tube, the signals of CuMoO$_4$ basically disappear. Based on the above analysis, CuMoO$_4$ is closely related to the activation process of methane. For the conversion of methane to methanol, CuMoO$_4$ is an important active component, which provides sufficient active sites. This conclusion also explains the phenomena in Fig. 7A and B very well, which in turn further validates the role of CuMoO$_4$.

3.4. Electronic states

The electronic states of elements on the catalyst surface were characterized by X-ray photoelectron spectroscopy (XPS). Mo 3d and O 1s XPS spectra of the four samples in different reaction situations are shown in Fig. 8 and the specific data are listed in Table S3.† Analyzing the Mo 3d XPS data, we can find four different binding energies appear in the spectra, which
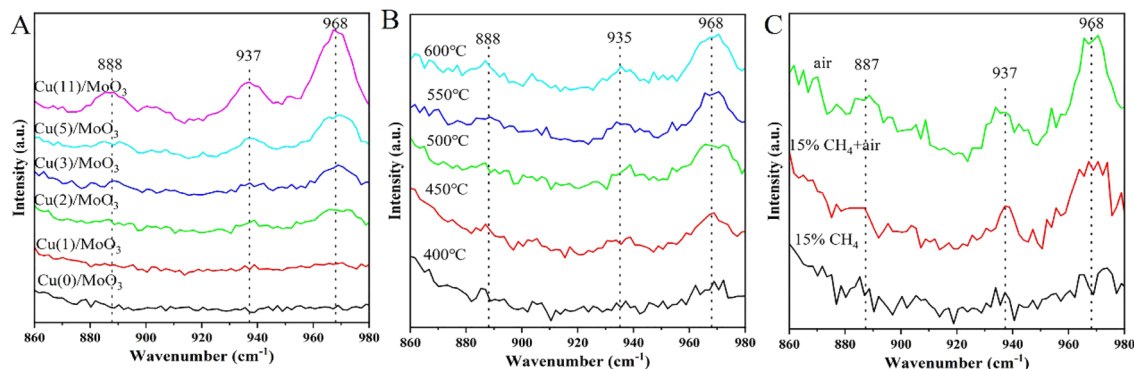

Fig. 7 (A) Raman spectra of various Cu loading. (B) Raman spectra of Cu(2)/MoO$_3$ at different temperature. (C) Raman spectra of Cu(2)/MoO$_3$ at 600 °C with different reaction gas.

correspond to 233.09 eV, 236.19 eV, 231.99 eV and 234.99 eV, respectively. Based on the conclusions of other articles,[53,69,70] the binding energies at 233.09 eV and 236.19 eV are assigned to Mo^{6+} $3d_{5/2}$ and Mo^{6+} $3d_{3/2}$. While the double hills at 231.99 eV and 234.99 eV can be regard as the orbital electrons of Mo^{5+} $3d_{5/2}$ and Mo^{5+} $3d_{3/2}$. In the light of the atomic ratios of Mo^{5+}/Mo^{6+}, we can demonstrate that molybdenum atoms with valence +6 dominate in Cu/MoO_3 catalyst. At the same time, this ratio is also closely related to the number of oxygen vacancies in the catalyst.[53,69] Under the calculation of Table S2,† the relationship between the atomic ratios of Mo^{5+}/Mo^{6+} for the four samples is expressed as (e) > (a) > (g) > (c). Therefore, the relationship between the number of oxygen vacancies for the four samples is also expressed as (e) > (a) > (g) > (c).

Conducting the same research on O 1s XPS data, two binding energies locating at 530.9 eV and 531.8 eV can be assigned to lattice oxygen (O_{lat}) and adsorbed oxygen (O_{ads}) on catalyst surface, respectively.[69,71] At the same time, the ratio of O_{ads}/O_{lat} usually signifies the number of oxygen vacancies. Judging by the Table S2,† the quantitative relationship of the four samples can be stated as (f) > (b) > (h) > (d). This result is similar to the previous conclusion obtained from Mo 3d XPS spectra. In the catalytic oxidation of methane, oxygen vacancies can usually assume the role of adsorbing and activating the reactive gas. Numerous studies have shown that the greater the number of oxygen vacancies, the generally better catalyst activity.[53,69,72,73] But comparing the XPS data of Cu(0)/MoO_3 and Cu(2)/MoO_3, we can find that the number of oxygen vacancies has decreased after Cu is impregnated on MoO_3 support. While the methane conversion together with methanol yield have enhanced remarkably. Obviously, supported Cu can form new active species with MoO_3, which could overcome the effects of reduced oxygen vacancies and increase the activity of methane oxidation simultaneously. During the preparation of catalysts, oxygen
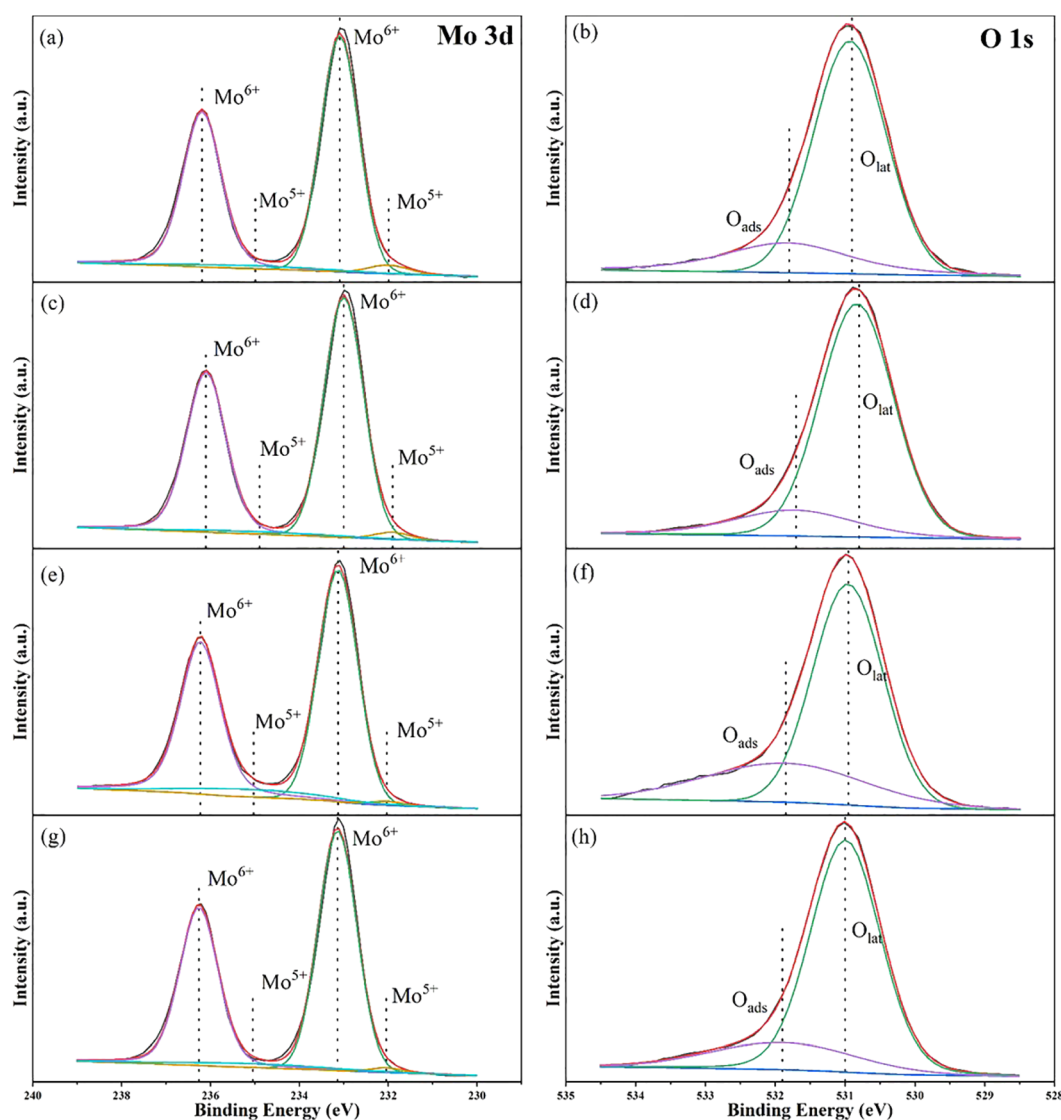

Fig. 8 Mo 3d and O 1s XPS spectra of (a) and (b) Cu(0)/MoO_3, (c) and (d): Cu(2)/MoO_3, (e) and (f) Cu(2)/MoO_3 before reaction at 600 °C, (g) and (h) Cu(2)/MoO_3 after reaction at 600 °C.

vacancies may play a role in trapping and immobilizing Cu elements.[74] The effect of reaction temperature can also be explained by the comparison of Fig. 8a, b, e and f. As the reaction temperature increased to 600 °C, the number of oxygen vacancies also increased. This maybe another reason why high temperature is beneficial to methanol yield. During the reaction process, oxygen vacancies help activate methane and oxygen. Wherefore, the number of oxygen vacancies decreases accordingly after the reaction, which is shown in Fig. 8g and h.

3.5. Reaction parameters optimization

Previous reaction studies have demonstrated the effect of Cu loading and reaction temperature on STY_{CH_3OH} and methanol selectivity. And the main target of this research is to achieve high methanol productivity. Hence, we had made efforts to optimize the molar ratio of $CH_4 : O_2 : H_2O$ to achieve methanol space-time yield improvement. Other articles have emphasized that the ratio of methane to oxygen has a stupendous effect on methanol yield.[43,60,75] So while keeping the proportion of water unchanged, we change the molar ratio of methane to oxygen to observe the effect on reactivity. The consequence is shown in Fig. 9a. As we can comprehend from the picture that with the increasing proportion of oxygen, the selectivity of methanol has been decreasing, but the space-time yield of methanol has first increased and then decreased. And the best molar ratio is 5 : 1.4 : 10, which helps the STY_{CH_3OH} to be maximized to 47.2 µmol g^{-1} h^{-1}. This phenomenon suggests that in order to achieve higher methanol space-time yield, the molar ratio of methane to oxygen should be appropriate. Too little oxygen is not conducive to the activation of the catalyst, resulting in less methanol production, while too much oxygen will cause more serious excessive oxidation, and it is not beneficial to the preservation of the methanol produced. Effect of the proportion of water on STY_{CH_3OH} and methanol selectivity is shown in Fig. 9b. Keeping the molar ratio of methane to oxygen unchanged and adjusting the water content gradually increased, the trend of STY_{CH_3OH} and methanol selectivity are identical with Fig. 9a. The amount of water in this experimental setup has been excessive, which inhibits the oxidation of methanol well, so the space-time yield

of methanol will initially increase. But when the content of water is several times that of methane and oxygen, too much water vapor can prevent methane and oxygen from coming into contact with the active site, thereby inhibiting methanol production. At the same time, the intermediate oxidation product $OHCH_2OOH$ will be better preserved, so the liquid phase selectivity of methanol will be reduced. Considering the STY_{CH_3OH}, molar ratio $CH_4 : O_2 : H_2O = 5 : 1.4 : 10$ is the best experimental conditions, while the best value is 47.2 µmol g^{-1} h^{-1}. Fig. 9c shows the stability test of Cu(2)/MoO₃ in the optimized condition. We can find that the STY_{CH_3OH} is slightly reduced and the selectivity of liquid products are almost unchanged. Therefore, the catalysts possess a certain stability.

3.6. Probable reaction mechanism

According to the above discussion, the probable reaction mechanism of methane oxidation to methanol is illustrated in Scheme 1. From the analysis on TS and Raman spectra, $CuMoO_4$ is the main active component, which is indispensable for the methane adsorption and C–H splitting. And other articles have convinced that methane is connected with Cu element, then the C–H bond would be broken.[43,50,52] Based on the result of ^{1}H-NMR, CH_3OH and CH_3OOH are the main liquid products, which proved that the methoxy formation is a significant step. Therefore, after methane is adsorbed at the active site, it will react with the nearby reactive oxygen species to form a methoxy group. Many articles have demonstrated that water has extraction and weak oxidation functions in methane-to-methanol reactions.[10,76,77] Thence, the methoxy group would convert to CH_3OH and CH_3OOH. After this step in the catalytic cycle, the active site will be inactivated, and the oxygen will mainly play a reactivation function and regenerate the catalyst activity. Thus, the probable reaction proceeds involve some basic steps as follows: (I) adsorption of methane molecule on the site of $CuMoO_4$; (II) dehydrogenation of methane molecule into CH_3^-; (III) the $-CH_3$ subsequently binds to the neighboring Cu attached O to form methoxy group; (IV) reaction with the OH^- species derived from water; (V) CH_3OH and CH_3OOH formation and desorption from Cu/MoO_3 interface; (VI) the
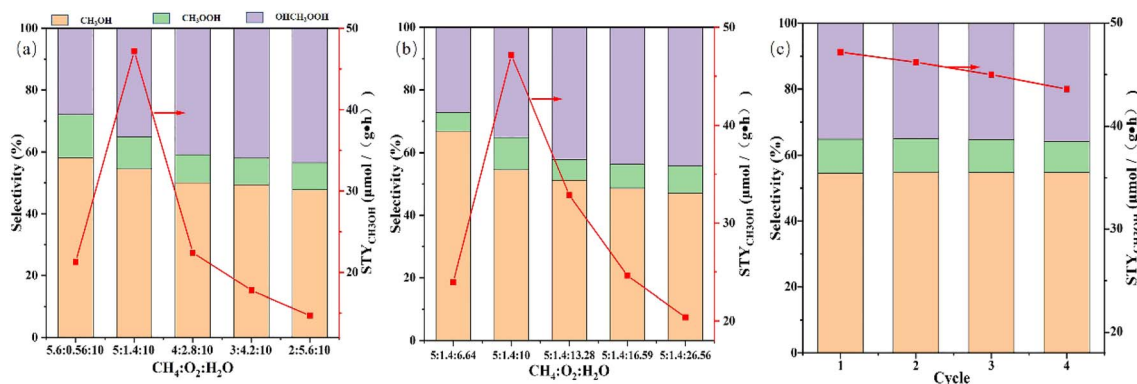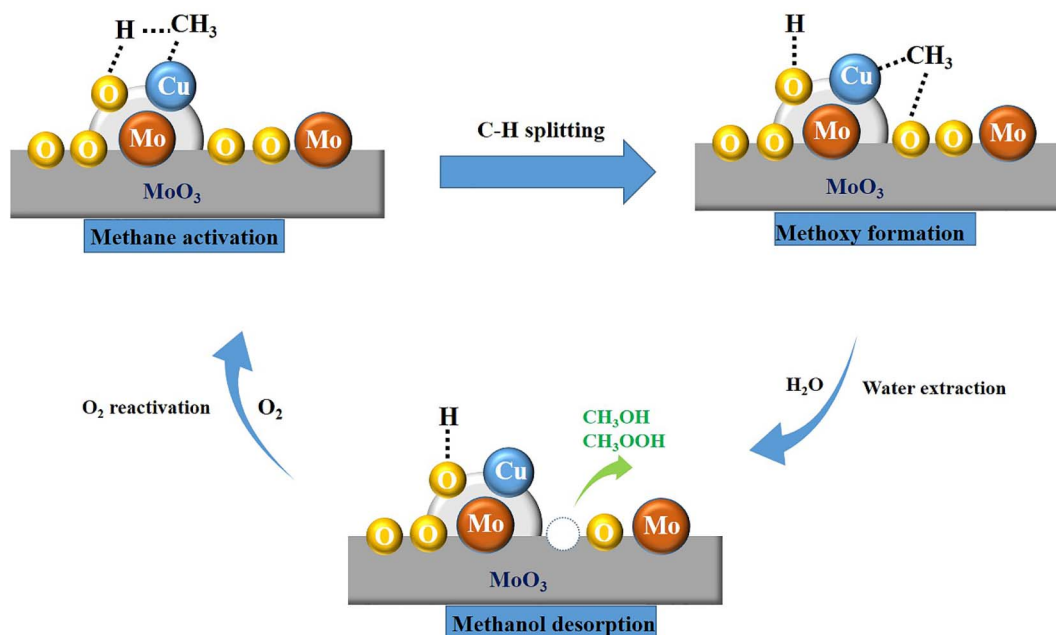

Fig. 9 (a) Effect of the molar ratio of $CH_4 : O_2$ on STY_{CH_3OH} and methanol selectivity of Cu(2)/MoO₃. Reaction conditions: $T = 600$ °C. (b) Effect of the proportion of water on STY_{CH_3OH} and methanol selectivity of Cu(2)/MoO₃. Reaction conditions: $T = 600$ °C. (c) Stability test of Cu(2)/MoO₃. Reaction conditions: $T = 600$ °C, $CH_4 : O_2 : H_2O = 5 : 1.4 : 10$.

Scheme 1 A probable oxidation mechanism of methane to methanol over Cu/MoO_3 catalyst.

catalyst activity is regenerated by O_2 to complete the catalytic pathway.

4. Conclusion

Cu/MoO_3 catalyst prepared by a simple impregnation method is capable of achieving direct continuous oxidation of methane to methanol in the gaseous phase. Analysis of XRD, TEM and SEM data shows that Cu is uniformly dispersed on the surface of MoO_3. And at the same time, it can interact with the carrier to form new species-$CuMoO_4$. The characterization techniques such as TS, Raman, XPS and H_2-TPR confirm the generation of $CuMoO_4$ and illustrate its important role as a provider of active sites in the methane oxidation reaction. The improvement of methanol yield is accomplished by adjusting a series of reaction parameters. The loading of Cu and reaction temperature have a significant impact on the reactivity. $Cu(2)/MoO_3$ catalyst reacted at 600 °C has the best performance among all experimental samples. Following by changing the molar ratio of $CH_4 : O_2 : H_2O$, methanol space-time yield reached its optimum value of 47.2 μmol g^{-1} h^{-1}. In the single-step oxidation of methane to methanol, this catalyst demonstrates a new carrier possibility. And with more improvements, it has tremendous potential to accomplish high yield of methanol.

Data availability

All relevant data are available from the authors on reasonable request.

Author contributions

Wenjian Wu: conceptualization, formal analysis and writing-original draft; Wenzhi Li: funding acquisition and writing-

review & editing; Mingwei Wu: writing-review & editing; Hao Zhang: software; Chen Zhu: investigation; Yihang Jiang: Investigation.

Conflicts of interest

The authors declare no conflicts of interest.

Acknowledgements

References

1 J. M. Chen, *Innov.*, 2021, **2**, 100127.

2 L. Chen, G. Msigwa, M. Yang, A. I. Osman, S. Fawzy, D. W. Rooney and P. S. Yap, *Environ. Chem. Lett.*, 2022, **20**, 2277–2310.

3 R. Wang and L. Guo, *IOP Conf. Ser. Earth Environ. Sci.*, 2020, **467**, 012069.

4 Y. Li and G. Veser, *Energy Technol.*, 2020, **8**, 2000460.

5 Q. Y. Duan, C. H. Zhang, S. Sun, Y. Pan, X. Zhou, Y. Liu, K. Chen, C. S. Li, X. Z. Wang and W. Z. Li, *J. Mater. Chem. A*, 2020, **8**, 7395–7404.

6 A. W. Petrov, D. Ferri, F. Krumeich, M. Nachtegaal, J. A. van Bokhoven and O. Kröcher, *Nat. Commun.*, 2018, **9**, 2545.

7 D. Kiani, S. Sourav, Y. Tang, J. Baltrusaitis and I. E. Wachs, *Chem. Soc. Rev.*, 2021, **50**, 1251–1268.

8 C. Karakaya and R. J. Kee, *Prog. Energy Combust. Sci.*, 2016, **55**, 60–97.

9 S. Bai, Y. Xu, P. Wang, Q. Shao and X. Huang, *ACS Catal.*, 2019, **9**, 6938–6944.

10 X. Tang, L. Wang, B. Yang, C. Fei, T. Y. Yao, W. Liu, Y. Lou, Q. G. Dai, Y. F. Cai, X. M. Cao, W. C. Zhan, Y. L. Guo, X. Q. Gong and Y. Guo, *Appl. Catal., B*, 2021, **285**, 119827.

11 W. N. Manan, W. N. R. Wan Isahak and Z. Yaakob, *Catalysts*, 2022, **12**, 452.

12 D. A. Hickman and L. D. Schmidt, *Science*, 1993, **259**, 343–346.

13 T. V. Choudhary and V. R. Choudhary, *Angew. Chem., Int. Ed.*, 2008, **47**, 1828–1847.

14 M. J. da Silva, *Fuel Process. Technol.*, 2016, **145**, 42–61.

15 S. J. Freakley, N. Dimitratos, D. J. Willock, S. H. Taylor, C. J. Kiely and G. J. Hutchings, *Acc. Chem. Res.*, 2021, **54**, 2614–2623.

16 M. H. Ab Rahim, M. M. Forde, R. L. Jenkins, C. Hammond, Q. He, N. Dimitratos, J. A. Lopez-Sanchez, A. F. Carley, S. H. Taylor, D. J. Willock, D. M. Murphy, C. J. Kiely and G. J. Hutchings, *Angew. Chem., Int. Ed. Engl.*, 2013, **52**, 1280–1284.

17 G. Qi, T. E. Davies, A. Nasrallah, M. A. Sainna, A. G. R. Howe, R. J. Lewis, M. Quesne, C. R. A. Catlow, D. J. Willock, Q. He, D. Bethell, M. J. Howard, B. A. Murrer, B. Harrison, C. J. Kiely, X. Zhao, F. Deng, J. Xu and G. J. Hutchings, *Nat. Catal.*, 2022, **5**, 45–54.

18 N. Agarwal, S. J. Freakley, R. U. McVicker, S. M. Althahban, N. Dimitratos, Q. He, D. J. Morgan, R. L. Jenkins, D. J. Willock, S. H. Taylor, C. J. Kiely and G. J. Hutchings, *Science*, 2017, **358**, 223–227.

19 J.-S. Min, H. Ishige, M. Misono and N. Mizuno, *J. Catal.*, 2001, **198**, 116–121.

20 Z. Jin, L. Wang, E. Zuidema, K. Mondal, M. Zhang, J. Zhang, C. Wang, X. Meng, H. Yang, C. Mesters and F. S. Xiao, *Science*, 2020, **367**, 193–197.

21 F. Gu, X. Qin, M. Li, Y. Xu, S. Hong, M. Ouyang, G. Giannakakis, S. Cao, M. Peng, J. Xie, M. Wang, D. Han, D. Xiao, X. Wang, Z. Wang and D. Ma, *Angew. Chem., Int. Ed. Engl.*, 2022, **61**, e202201540.

22 J. Shan, M. Li, L. F. Allard, S. Lee and M. Flytzani-Stephanopoulos, *Nature*, 2017, **551**, 605–608.

23 M. W. Li, J. J. Shan, G. Giannakakis, M. Y. Ouyang, S. F. Cao, S. Lee, L. F. Allard and M. Flytzani-Stephanopoulos, *Appl. Catal., B*, 2021, **292**, 120124.

24 R. Sharma, H. Poelman, G. B. Marin and V. V. Galvita, *Catalysts*, 2020, **10**, 194.

25 Z. Zakaria and S. K. Kamarudin, *Renew. Sustain. Energy Rev.*, 2016, **65**, 250–261.

26 M. Alvarez, P. Marin and S. Ordonez, *Mol. Catal.*, 2020, **487**, 110886.

27 S. Grundner, M. A. Markovits, G. Li, M. Tromp, E. A. Pidko, E. J. Hensen, A. Jentys, M. Sanchez-Sanchez and J. A. Lercher, *Nat. Commun.*, 2015, **6**, 7546.

28 A. Martini, M. Signorile, C. Negri, K. Kvande, K. A. Lomachenko, S. Svelle, P. Beato, G. Berlier, E. Borfecchia and S. Bordiga, *Phys. Chem. Chem. Phys.*, 2020, **22**, 18950–18963.

29 M. Mao, L. Liu and Z. Liu, *Molecules*, 2022, **27**, 7146.

30 D. T. Bregante, L. N. Wilcox, C. Liu, C. Paolucci, R. Gounder and D. W. Flaherty, *ACS Catal.*, 2021, 11873–11884, DOI: **10.1021/acscatal.1c03471**.

31 J. Ohyama, Y. Tsuchimura, A. Hirayama, H. Iwai, H. Yoshida, M. Machida, S. Nishimura, K. Kato and K. Takahashi, *ACS Catal.*, 2022, **12**, 2454–2462.

32 A. Hirayama, Y. Tsuchimura, H. Yoshida, M. Machida, S. Nishimura, K. Kato, K. Takahashi and J. Ohyama, *Catal. Sci. Technol.*, 2021, **11**, 6217–6224.

33 B. Michalkiewicz, *Appl. Catal., A*, 2004, **277**, 147–153.

34 B. Wu, T. J. Lin, Z. X. Lu, X. Yu, M. Huang, R. O. Yang, C. Q. Wang, C. Tian, J. Li, Y. H. Sun and L. S. Zhong, *Chem*, 2022, **8**, 1658–1672.

35 G. N. Li, P. Vassilev, M. Sanchez-Sanchez, J. A. Lercher, E. J. M. Hensen and E. A. Pidko, *J. Catal.*, 2016, **338**, 305–312.

36 G. Y. Zhao, E. Benhelal, A. Adesina, E. Kennedy and M. Stockenhuber, *J. Phys. Chem. C*, 2019, **123**, 27436–27447.

37 J. R. Anderson and P. Tsai, *J. Chem. Soc., Chem. Commun.*, 1987, 1435–1436, DOI: **10.1039/c39870001435**.

38 T. Yu, Z. Li, L. Lin, S. Q. Chu, Y. Su, W. Y. Song, A. Q. Wang, B. M. Weckhuysen and W. H. Luo, *ACS Catal.*, 2021, **11**, 6684–6691.

39 T. Yu, Y. Su, A. Wang, B. M. Weckhuysen and W. Luo, *Chemcatchem*, 2021, **13**, 2766–2770.

40 Y. K. Chow, N. F. Dummer, J. H. Carter, C. Williams, G. Shaw, D. J. Willock, S. H. Taylor, S. Yacob, R. J. Meyer, M. M. Bhasin and G. J. Hutchings, *Catal. Sci. Technol.*, 2018, **8**, 154–163.

41 M. V. Parfenov, E. V. Starokon, L. V. Pirutko and G. I. Panov, *J. Catal.*, 2014, **318**, 14–21.

42 H. V. Le, S. Parishan, A. Sagaltchik, H. Ahi, A. Trunschke, R. Schomäcker and A. Thomas, *Chem.–Eur J.*, 2018, **24**, 12592–12599.

43 S. E. Bozbag, P. Sot, M. Nachtegaal, M. Ranocchiari, J. A. van Bokhoven and C. Mesters, *ACS Catal.*, 2018, **8**, 5721–5731.

44 Z. Liu, E. Huang, I. Orozco, W. Liao, R. M. Palomino, N. Rui, T. Duchon, S. Nemsak, D. C. Grinter, M. Mahapatra, P. Liu, J. A. Rodriguez and S. D. Senanayake, *Science*, 2020, **368**, 513–517.

45 M. T. Greiner, L. Chai, M. G. Helander, W. M. Tang and Z. H. Lu, *Adv. Funct. Mater.*, 2013, **23**, 215–226.

46 Y. Zhu, Y. Yao, Z. Luo, C. Pan, J. Yang, Y. Fang, H. Deng, C. Liu, Q. Tan, F. Liu and Y. Guo, *Molecules*, 2019, **25**, 18.

47 H. F. Liu, R. S. Liu, K. Y. Liew, R. E. Johnson and J. H. Lunsford, *J. Am. Chem. Soc.*, 1984, **106**, 4117–4121.

48 K. Aoki, M. Ohmae, T. Nanba, K. Takeishi, N. Azuma, A. Ueno, H. Ohfune, H. Hayashi and Y. Udagawa, *Catal. Today*, 1998, **45**, 29–33.

49 C. Brookes, P. P. Wells, G. Cibin, N. Dimitratos, W. Jones, D. J. Morgan and M. Bowker, *ACS Catal.*, 2014, **4**, 243–250.

50 J. Zhu, F. Gao, L. Dong, W. Yu, L. Qi, Z. Wang, L. Dong and Y. Chen, *Appl. Catal., B*, 2010, **95**, 144–152.

51 T. Akiyama, R. Sei and S. Takenaka, *Catal. Sci. Technol.*, 2021, **11**, 5273–5281.

52 S. Patnaik, G. Swain and K. M. Parida, *Nanoscale*, 2018, **10**, 5950–5964.

53 B. Tang, W. Li, X. Zhang, B. Zhang, H. Zhang and C. Li, *Fuel*, 2022, **324**, 124674.

54 W. G. Cortés Ortiz, D. Delgado, C. A. Guerrero Fajardo, S. Agouram, R. Sanchís, B. Solsona and J. M. López Nieto, *Mol. Catal.*, 2020, **491**, 110982.

55 A. Wang and L. Olsson, *Chem. Eng. J.*, 2020, **395**, 125048.

56 Q. Lin, J. Liu, S. Liu, S. Xu, C. Lin, X. Feng, Y. Wang, H. Xu and Y. Chen, *Dalton Trans.*, 2018, **47**, 15038–15048.

57 J. L. Brito, J. Laine and K. C. Pratt, *J. Mater. Sci.*, 1989, **24**, 425–431.

58 W. Yu, J. Zhu, L. Qi, C. Sun, F. Gao, L. Dong and Y. Chen, *J. Colloid Interface Sci.*, 2011, **364**, 435–442.

59 A. A. Latimer, A. Kakekhani, A. R. Kulkarni and J. K. Norskov, *ACS Catal.*, 2018, **8**, 6894–6907.

60 T. Takemoto, D. He, Y. Teng, K. Tabata and E. Suzuki, *Appl. Catal., A*, 2002, **225**, 177–184.

61 J. S. Woertink, P. J. Smeets, M. H. Groothaert, M. A. Vance, B. F. Sels, R. A. Schoonheydt and E. I. Solomon, *Proc. Natl. Acad. Sci. U. S. A.*, 2009, **106**, 18908–18913.

62 P. J. Smeets, M. H. Groothaert and R. A. Schoonheydt, *Catal. Today*, 2005, **110**, 303–309.

63 L. Huang, H. Xu, R. Zhang, X. Cheng, J. Xia, Y. Xu and H. Li, *Appl. Surf. Sci.*, 2013, **283**, 25–32.

64 P. C. H. Mitchell and F. Trifiro, *J. Chem. Soc. A*, 1970, 3183–3188.

65 U. Steiner, T. Morgenstern, W. Reichelt, H. Borrmann and A. Simon, *Z. fur Anorg. Allg. Chem.*, 1994, **620**, 1905–1908.

66 B. Zhang, S. T. Xiang, A. I. Frenkel and I. E. Wachs, *ACS Catal.*, 2022, **12**, 3226–3237.

67 P. Chen, Z. Xie, Z. Zhao, J. Li, B. Liu, B. Liu, X. Fan, L. Kong and X. Xiao, *Catal. Sci. Technol.*, 2021, **11**, 4083–4097.

68 B. Saravanakumar, G. Ravi, R. Yuvakkumar, V. Ganesh and R. K. Guduru, *Mater. Sci. Semicond. Process.*, 2019, **93**, 164–172.

69 L. Xu, W. Zhou, S. Chao, Y. Liang, X. Zhao, C. Liu and J. Xu, *Adv. Energy Mater.*, 2022, **12**, 2200101.

70 Q. L. Wu, S. X. Zhao, L. Yu, X. X. Zheng, Y. F. Wang, L. Q. Yu, C. W. Nan and G. Z. Cao, *J. Mater. Chem. A*, 2019, **7**, 13205–13214.

71 G. Wei, Z. Zhou, X. Zhao, W. Zhang and C. An, *ACS Appl. Mater. Interfaces*, 2018, **10**, 23721–23730.

72 K. Chen, W. Z. Li, Z. A. Zhou, Q. F. Huang, Y. Liu and Q. Y. Duan, *Catal. Sci. Technol.*, 2020, **10**, 2573–2582.

73 Y. Jiang, W. Li, K. Chen, X. Zhang, C. Shen and L. Yuan, *Mol. Catal.*, 2022, **522**, 112229.

74 J. F. Chen, X. Y. Wang, L. L. Zhang and Z. B. Rui, *Appl. Catal., B*, 2021, **297**, 120410.

75 L. L. Sun, Y. Wang, C. M. Wang, Z. K. Xie, N. J. Guan and L. D. Li, *Chem*, 2021, **7**, 1557–1568.

76 B. Wu, T. Lin, M. Huang, S. Li, J. Li, X. Yu, R. Yang, F. Sun, Z. Jiang, Y. Sun and L. Zhong, *Angew. Chem., Int. Ed.*, 2022, **61**, e202204116.

77 V. L. Sushkevich, D. Palagin, M. Ranocchiari and J. A. van Bokhoven, *Science*, 2017, **356**, 523–527.